The Structure of Water Under Confinement in Periodic Mesoporous Organosilicas Investigated by X-Ray Scattering

Niels Christian Gießelmann,[†] Philip Lenz,[‡,¶] Sophia-Marie Meinert,[‡] Tamás Simon,[‡] Wonhyuk Jo,[†,§] Nele Naomi Striker,[†] Michael Fröba,[*,‡,¶] and Felix Lehmkühler[*,†,¶]

†*Deutsches Elektronen-Synchrotron DESY, Notkestr. 85, 22607 Hamburg, Germany*

‡*University of Hamburg, Institute of Inorganic and Applied Chemistry,*
Martin-Luther-King-Platz 6, 20146 Hamburg, Germany

¶*The Hamburg Centre for Ultrafast Imaging, Luruper Chaussee 149, 22761 Hamburg, Germany*

§*European XFEL, Holzkoppel 4, 22869 Schenefeld, Germany*

E-mail: michael.froeba@uni-hamburg.de; felix.lehmkuehler@desy.de

Abstract

The effect of pore wall chemistry and pore diameter on the structure of confined water was studied by X-ray scattering on water confined in periodic mesoporous organosilicas (PMOs). A shift in the first structure factor peak at $q \approx 1.8\,\mathrm{\AA}^{-1}$ reveals a variation in the density of the confined water in dependence of hydrophilicity and pore size. Smaller and more hydrophilic pores induce a lower density in the water. In contrast to bulk water, the pair distribution functions (PDFs) of confined water show a splitting of the second-neighbour peak into either two, in the case of smaller and more hydrophilic pores, or three separate peaks, in larger and more hydrophobic pores. From the running coordination number we conclude that smaller and more hydrophilic confinement leads to a stronger developed tetrahedral network in confined water, while confinement in larger and hydrophobic pores give tetrahedral arrangements that are bulk-like or even less pronounced than in bulk water.

Introduction

Liquid water is known to show different equilibrium and dynamical properties in spatial confinement compared to bulk.[1–9] One particular example of this is a lower melting temperature compared to bulk water in dependence of the dimensions of the confining space.[1–4]

When confined in nanometer-sized pores, it has been found that the structure of water is not homogeneous throughout the pore: At the interface between the water and the surrounding material a layer of a thickness of two to three molecules forms, which has a higher density than the water in the pore center.[10–13] This interfacial layer is also sometimes called the non-freezing layer, as it does not form a crystalline structure upon freezing.[1,3] A remarkable finding by Soper *et al.*[12,14] has been that, while the interfacial layer in MCM-41 shows a higher and the core water a lower density than bulk water, the average density throughout the whole pore cross-section is lower than that of bulk water. This could be explained by a high negative pressure that the water experiences inside the pore. Soper[14] suggests that this negative pressure is caused by the formation of a concave meniscus where the liquid water inside the pore meets the water vapour on the outside.

Table 1: List of porous materials used in the experiment. Shown are the synthesis precursor, the pore diameter d_P (where the uncertainty is given by the half width at half maximum of the pore size distribution), the pore volume at $90\,\%$ relative pressure $V_{P,0.9}$, the BET surface area $S_\mathbf{BET}$, the organic unit periodicity $d_\mathbf{org}$ and where applicable the capillary condensation onset $(p/p_0)_\mathbf{onset}$, the number of water molecules per area $N_\mathbf{w}$. and the slope of the water adsorption isotherm for $p/p_0 < 0.5$.

	Precursor	d_P [nm]	$V_{\mathrm{P},0.9}$ [cm^{3}g^{-1}]	S_BET [m^{2}g^{-1}]	d_org [nm]	$(p/p_0)_\mathrm{onset}$	N_w [nm^{-2}]	$s_{<0.5}$ [cm^{3}g^{-1}]
■	MCM-41	3.9±0.3	0.85	956	-	0.52	3.7	232
✚	BTEVB	3.8±0.7	0.54	762	1.19	0.75	0.96	31
●	BTEVFB	4.9±1.4	0.83	632	1.20	-	-	-
►	BTEVFB	4.4±0.7	1.04	976	1.20	0.88	0.66	24
▲	BTEVA	4.3±0.3	0.83	966	1.18	-	-	-
◄	BTEVA	3.8±0.4	0.67	948	1.18	0.67	2.0	104
◆	BTEVA	3.4±0.4	0.64	929	1.18	-	-	-
✖	BTEVP	3.5±0.8	0.63	851	1.19	0.56	1.7	90

Studies considering the molecular structuring of water under nanoscale confinement have also previously been conducted, using methods such as X-ray and neutron scattering,[15,16] as well as Raman spectroscopy.[17,18] There are also a number of simulation studies on the topic.[10,12,14] Authors employing different methods arrive at varying conclusions, in particular in regards to the effect of confinement on the amount of tetrahedral structuring. Crupi *et al.*[17] and Malfait *et al.*,[18] for example, found a decrease in strongly hydrogen-bonded, tetrahedral structures in the confined water, while previous studies using scattering techniques observed an increase of these structures.[15,16] Simulation studies, for example by Soper *et al.*[12,14] also found an increase of tetrahedrally structured water under confinement.

In order to investigate the influence of different parameters on the structure of confined water, we analyze its structure in materials with varying pore diameter and pore wall chemistry. This is achieved by the use of periodic mesoporous organosilicas. These are a class of material consisting of a SiO_2 base lattice with periodically arranged organic moieties in the pore walls, forming a crystal-like wall structure.[19–26] The organic moieties can furthermore host functional components of various kinds, which can alter the interaction between the pore walls and the confined material.[27,28] PMOs provide a high stability due to the inorganic part and at the same time a wide variety of possible functionalities in the organic bridging unit and can therefore be tuned to various intended applications, such as catalysis,[29,30] drug delivery[31,32] or light harvesting.[33–35] Tuning the pore-water interaction and polarity of the pore wall has an influence on the structure and dynamics of water confined in PMOs.[18,26,28,36,37]

For instance, using Raman spectroscopy to investigate the hydrogen bonding behaviour in water confined in PMOs, a reduction of tetrahedrally H-bonded was found in both MCM-41 and a more hydrophobic, phenylene-bridged BTEB-PMO with the effect being more pronounced in the latter.[18]

Another study by Jani *et al.*[28] claims that the dynamics of water are slowed down in the case of PMO confinement. Here, the diffusivity of water molecules close to the PMO interface is slower in the case of hydrophilic groups in the pore wall compared to hydrophobic ones.

With the study at hand, we want to expand the insight into the behaviour of water in these systems by conducting X-ray scattering experiments on a variety of PMO materials, covering several pore sizes and pore wall functionalizations. This technique grants us direct access to the structural information of PMO-confined water, while a large selection of PMO materials allows us to study the impact of varying hydrophilicity over pore diameters between 3.5 and 5 nm. By studying the structure factors, pair distribution functions and coordination numbers of water confined in PMOs, we find indications for a lower density and more strongly developed tetrahedral network under hydrophilic confinement when compared to bulk. This effect is strongly material-dependent and is amplified by confinement in smaller pores.

Sample characterisation We used a variety of PMOs, as well as pure mesoporous silica (MCM-41), in order to cover different variations in pore diameter and pore wall functionalization. The precursors used for the PMO synthesis are 2,5-bis((*E*)-2-(triethoxysilyl)-

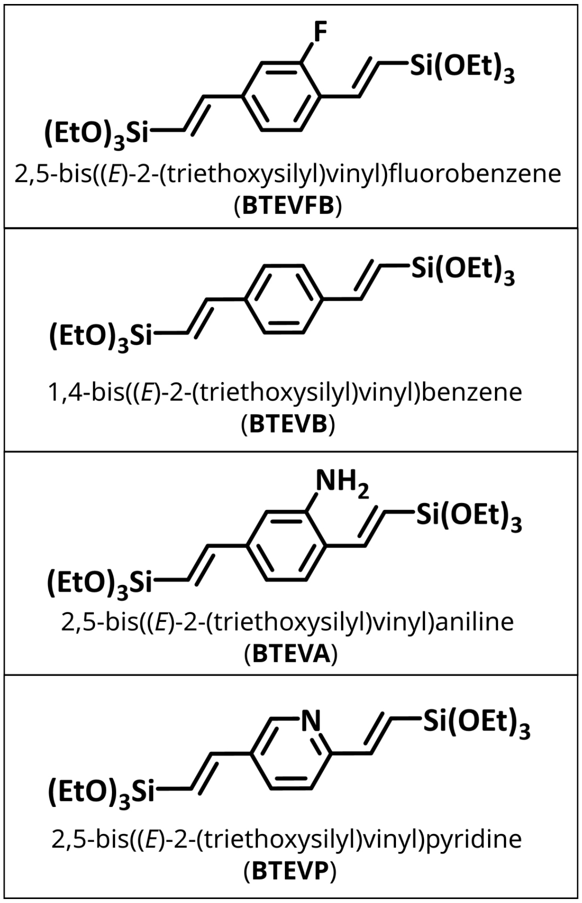

2,5-bis((*E*)-2-(triethoxysilyl)vinyl)fluorobenzene
(**BTEVFB**)

1,4-bis((*E*)-2-(triethoxysilyl)vinyl)benzene
(**BTEVB**)

2,5-bis((*E*)-2-(triethoxysilyl)vinyl)aniline
(**BTEVA**)

2,5-bis((*E*)-2-(triethoxysilyl)vinyl)pyridine
(**BTEVP**)

Figure 1: Chemical structures of the precursors.

vinyl)fluorobenzene (BTEVFB), 1,4-bis((*E*)-2-(triethoxysilyl)vinyl)benzene (BTEVB), 2,5-bis((*E*)-2-(triethoxysilyl)vinyl)aniline (BTEVA) and 2,5-bis((*E*)-2-(triethoxysilyl)vinyl)pyridine (BTEVP). The chemical strucure of the precursors is shown in Figure 1 and a list of the porous materials and their most important properties for this study is given in Table 1. More details on the material properties are found in the supplementary information. In this study, the notation of the PMOs will be the precursor followed by the pore diameter in nanometers written in parentheses. For example, BTEVA(3.4) denotes the PMO prepared with the BTEVA precursor and with a pore diameter of 3.4 nm.

Details of the PMO synthesis, including a table with the synthesis parameters, are given in the supplementary information. In short, the synthesis of the BTEVB,[26,38] BTEVA[26] and BTEVFB[24,38] precursors and their reaction to the corresponding PMOs were carried out according to the synthesis instructions given in literature. The synthesis of the BTEVP precursor is a modified form of literature synthesis.[23] Deviating from the three-step synthesis in the second step, the preparation of 2,5-diethynylpyridine, was carried out in a modified way.[39]

Nitrogen physisorption measurements were performed to characterize the porosity of the different materials. At first, the samples were activated at 100 °C for 20 h under reduced pressure in a degasser (*Quantachrome Masterprep*). The N_2-physisorption measurements were performed at a temperature of 77 K (*Quantachrome Quadrasorb-SI-MP* and *Quadrasorb evo*). Using the program *QuadraWin 6.0*, the pore size distribution according to density functional theory (DFT) calculation with the model N_2 on silica (cylindr. pores, non-local DFT (NLDFT) at adsorptions branch and the specific surface area with the Brunauer–Emmett–Teller (BET) method (p/p_0 range from 0.05 to 0.3) were determined from the obtained measurement.[40–42] In case of the intersection of the BET region with the condensation step of the isotherms, the BET range was reduced in order to be in the plateau region before the condensation ($p/p_0 < 0.3$). The measured nitrogen physisorption isotherms and the calculated pore size distribution of all materials are shown in Fig. 2A. A type IV(b)-

N_2 physisorption isotherm can be observed for all materials except for BTEVFB(4.9), which has hysteresis caused by cavitation or pore blocking effects and thus shows a type IV(a) isotherm.[42] Some of the porosity data of the different materials determined from the N_2 isotherms are listed in Table 1.

For the investigation of materials with regard to their hydrophilicity, the use of water as an adsorptive is suitable due to its sensitivity to surface chemistry.[26,36,43–45] To perform the water vapor sorption measurements, the samples were first degassed at 100 °C for 20 hours (*Quantachrome MasterPrep Degasser*). Water vapor sorption isotherms were recorded at 25 °C (*Quantachrome VSTAR*™).

Information on hydrophilicity can be obtained from water vapor sorption isotherms using the onset before the capillary condensation step, as well as the slope of the isotherm in the region of $p/p_0 < 0.5$. Since the relative pressure region of the onset is determined not only by the chemistry of the material surface but also by the pore radius, materials with similar pore diameters should be compared for the determination of hydrophilicity (see Fig. 2B). For materials with the same pore diameter, more hydrophilic materials take more water at lower relative pressures, so capillary condensation occurs at lower relative pressures than for more hydrophobic materials.[26]

In the relative pressure range $p/p_0 < 0.5$, the pure silica MCM-41(3.9) has the steepest slope. As can be seen in Table 1, the onset of pore condensation of MCM-41(3.9) has the smallest value. BTEVB(3.8) has by far the lowest slope and the highest onset position of the capillary condensation, indicating a comparatively higher hydrophobicity. In addition, it does not reach a plateau level after condensation, thus the pores are not completely filled even at higher relative pressures. BTEVA(3.8) and BTEVP(3.5) are found between the samples mentioned above. While both have a similar slope, BTEVP(3.5) has a lower onset position with $p/p_0 = 0.56$ than the BTEVA(3.8) with $p/p_0 = 0.67$.

The amount of water adsorbed at the onset can be used to calculate the number of water molecules per surface area (N_w).[1,26] Comparing the different values for N_w (see Table 1)

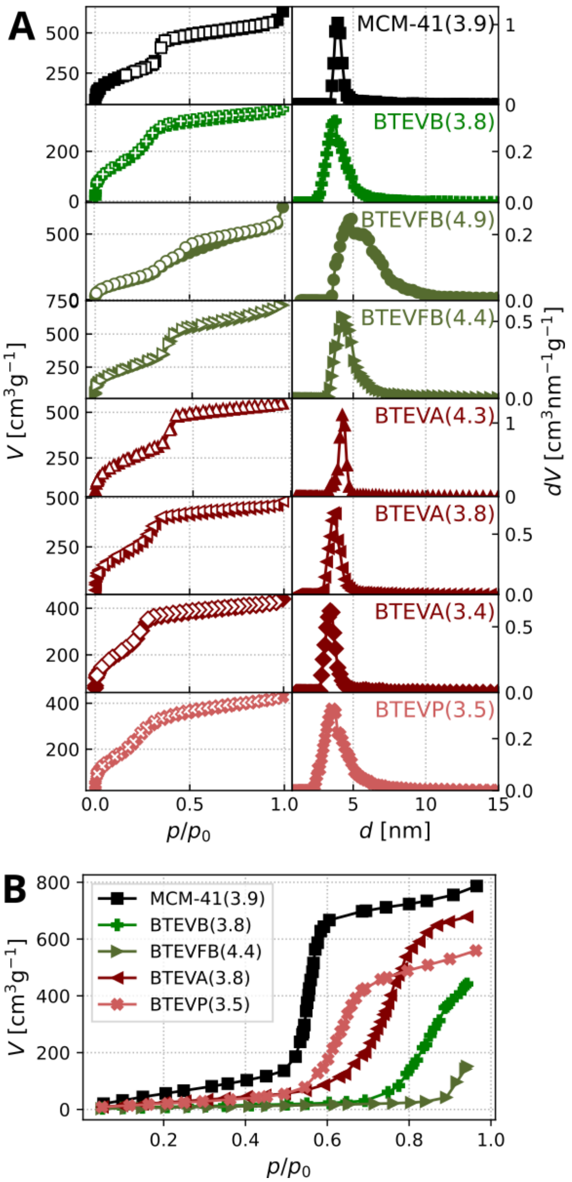

Figure 2: **A** The N_2 physisorption isotherms (77 K) of the samples (left), showing adsorption (filled symbols) and desorption (hollow symbols). On the right the pore size distribution curves, calculated using DFT. **B** Water vapor sorption isotherms at 25°C of the adsorption branches from the materials with a pore diameter of about 3.8 nm. Additionally, the fluorinated BTEVFB sample with a pore diameter of 4.4 nm is shown.

MCM-41 has $N_\mathrm{w} = 3.7$ water molecules per square nanometer, which is also in agreement with the literature value.[1] The divinylaniline and -pyridine materials show similar values with $N_\mathrm{w} = 2.0$ and $N_\mathrm{w} = 1.7\,\mathrm{nm}^{-2}$, respectively. Among the materials with pores about 3.8 nm in size, the divinylbenzene bridged PMO has the lowest density of water molecules on the surface with $N_\mathrm{w} = 0.96\,\mathrm{nm}^{-2}$. Additionally, a fluorine-containing PMO with a slightly larger pore diameter of 4.4 nm is shown. As with the divinylbenzene bridged PMOs, no plateau of the condensation step is achieved even at higher relative pressures. Since this material has the lowest slope and water density on the surface, it can be classified as the most hydrophobic among the presented materials. From the water vapor sorption analysis, the following series can be established, in which the hydrophilicity increases from left to right:

BTEVFB $<$ BTEVB $<$ BTEVA $\leq$ BTEVP $<$ MCM-41

Experiment and analysis The total X-ray scattering measurement was performed at the P02.1 beamline at DESY[46] with a beam diameter of approximately 1 mm and at an energy of 60 keV. The powder samples were filled into glass capillaries with a diameter of 1.5 mm and a wall thickness of 10 µm (*Hilgenberg GmbH*). Scattering patterns were taken at temperatures between 290 and 245 K with an exposure time of 1 s. LaB_6 was used as a calibration sample for the measurements. The cooling was controlled by a nitrogen cryostream surrounding the sample capillary. We estimated the error of the temperature conservatively at 5 K, which is implied in all temperature data we measured.

The water was adsorbed into the PMOs by means of a humidity chamber where the humidity was gradually increased, thereby achieving a complete filling of the pores. Both the water-filled and empty PMOs were investigated. This way, the water signal could be isolated by subtracting the signal of the empty PMO from the filled one. Because the electron density of the water molecule is mostly located at the oxygen atom, this is the dominant contributor to the X-ray scattering signal. As typical for X-ray studies, the quantities we compute do therefore not contain information about the bonding between the oxygen and hydrogen atoms but only about the oxygen structure.[47] To discuss the structure of the confined water, we make use of the (total) structure factor $S(q)$, which can be computed as described by Juhás *et al.*:[48]

$$S(q) = \frac{I_c(q) - \langle f(q)^2 \rangle + \langle f(q) \rangle^2}{\langle f(q) \rangle^2}. \tag{1}$$

Here, I_c is the coherent scattering intensity and $f(q)$ the atomic scattering factor. In order to compute the coherent contribution of the scattering intensity, corrections have to be applied which are further described by Juhás et al,[48] as well as Egami and Billinge.[49] For the discussion of $S(q)$ we will focus on the region of q between 1.5 to about $4\,\text{Å}^{-1}$. In this region bulk water typically shows two peaks, the first of which shifts to smaller q upon cooling. The subsequent spread of the two peaks can be used as a measure of the amount of tetrahedrally structured water in bulk.[50,51] However, in confinement other factors must also be taken into account, such as interface interactions and geometric constraints, as these also affect the structuring of confined water.[10–12,14,15] From the structure factor the pair disribution functions (PDFs) can be computed as

$$G(r) = \frac{2}{\pi} \int\limits_{q_{min}}^{q_{max}} q[S(q) - 1] \sin qr \, \mathrm{d}q. \tag{2}$$

$S(q)$ and the PDF were computed using the *PDFGetX3* software.[48] Another interesting quantity is the running coordination number n_{OO}.[14,52,53] It is calculated via the r-weighted integral of the reduced PDF,

$$n_{\mathrm{OO}}(r) = \int\limits_{0}^{r} r' g(r') \, \mathrm{d}r', \tag{3}$$

with $g(r) = G(r) - 1$. n_{OO} gives the coordination number at a distance r from the origin

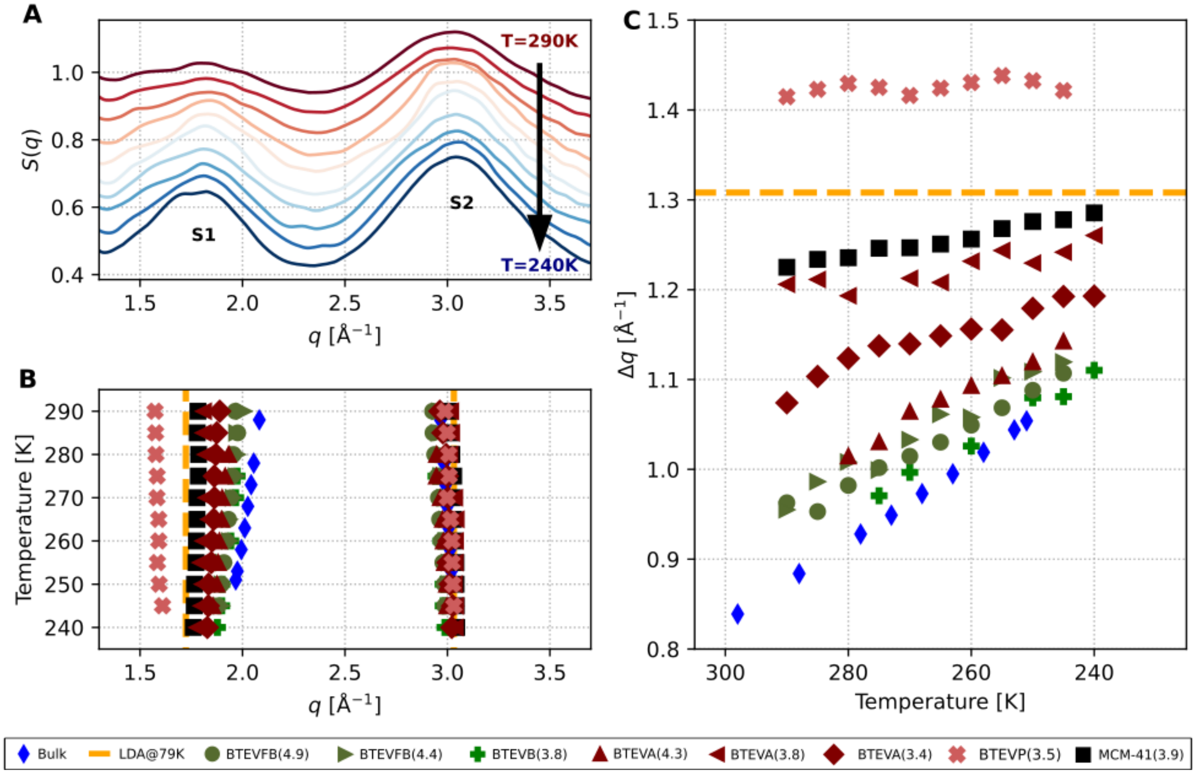

Figure 3: **A** The structure factor $S(q)$ of water in BTEVA(3.8)-PMO from 290 K (top) to 240 K (bottom) as an example of the typical form of the structure factor. **B** The structure factor peaks over different temperatures for water in different PMOs as well as in bulk. The bulk data was obtained from Sellberg *et al.*[50] **C** The splitting Δq between the $S(q)$ peaks. The LDA value was obtained from Mariedahl *et al.*[52]

atom.

Results

Structure factor Figure 3A exemplary shows the structure factor of water confined in BTEVA(3.8)-PMO at temperatures between 290 and 240 K. During cooling both a spread and a growth of the two peaks is observed. This is a typical behaviour reported for water. In bulk water this peak spread is often attributed to a more pronounced formation of a tetrahedral and hydrogen-bonded structure between the water molecules.[50,51] However, in confinement other interactions, like those between the water molecules and the pore wall, also have a considerable influence on the structuring of the molecules.[10–12,14,15]

Figure 3B shows the position of the structure factor peaks for different PMOs, as well as bulk water. The peak spread occurs in almost all samples with the exception of BTEVP(3.8). Here the lower-q peak (S1) seems to shift to larger q rather than lower ones.

The spread of the peaks during cooling, *i.e.* the difference between the two peak positions, can be observed in Fig. 3C. A strong dependence of the peak spread Δq on the confining material is found. Bulk water consistently shows the smallest values for Δq, while also giving rise to the strongest increase of the spread during the cooling process. The hydrophobic samples, which are shown with green markers in the figures, show a slightly larger spread and smaller increase for lowering temperature. The hydrophilic PMOs, as well as MCM-41(3.9), marked in red and black, respectively, show the largest Δq but cause a smaller change during cooling. BTEVP(3.5) shows the most extreme behaviour compared to bulk water by staying at almost a constant value for Δq throughout the cooling process.

In the further discussion of the structure factor, we will focus only on the position of the first peak (S1), as the second peak does not show a strong dependence on the different confinement, as well as bulk conditions. This reduces the statistical error compared to the difference between the peak positions.

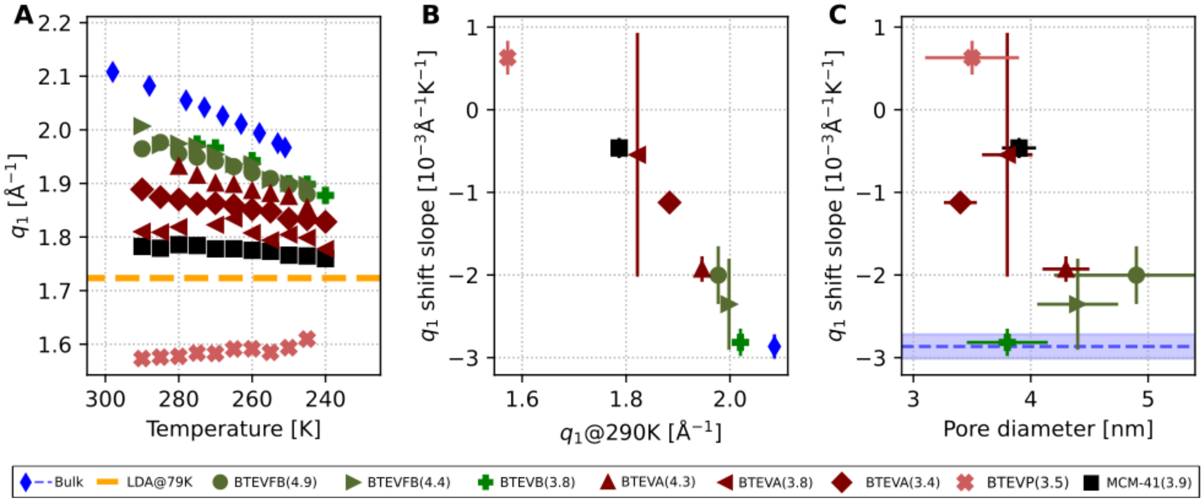

Figure 4: **A** The position of the first structure factor peaks in various materials over temperature. **B** The slope of the linearly fitted peak shift against the peak position at 290 K of the same fit. **C** The slope of the linearly fitted peak shift against the pore size.

These S1 positions q_1 are shown in Fig. 4A. A roughly linear behaviour is found in all samples, with the slopes depending on the type of porous material. At room temperature, bulk water shows the highest q_1, which then decreases the most throughout the cooling process. Next to the bulk water are the rather hydrophobic materials BTEVB and BTEVFB, the latter of which were measured with two different pore diameters of 4.9 and 4.4 nm. At lower q, we then find more hydrophilic samples including BTEVA with different pore diameters, as well as MCM-41(3.9). These also show a smaller slope than bulk water and the more hydrophobic samples. BTEVP(3.5) shows a different behaviour than the other samples with the lowest q_1 at room temperature, which then increases with lower temperatures. A shift of S1 to smaller q in water under confinement has consistently been reported in previous studies as well.[14,54,55]

Figure 4A also shows the q_1-value for low density amorphous ice (LDA), as measured by Mariedahl *et al.*[52] It provides a fitting reference when comparing structural features in this context, as it has a strongly tetrahedral structure without interstitials.[52,56] In our study, all samples seem to approach the value of low density amorphous ice (LDA) when cooling, including BTEVP(3.5). In this sample, S1 starts in fact at a lower q_1 than LDA and then rises upon cooling, thereby also approaching the value of LDA. Note also that water under confinement has a smaller q_1 than bulk water for all observed materials and temperatures.

Fig. 4A suggests a correlation between the slope of the linearly fitted peak shift and the peak position at room temperature. This relationship is shown in Fig. 4B. Here, a clear trend with regard to material hydrophilicity is observed. At room temperature, q_1 is at lower values for hydrophilic samples, while the slopes of their S1 shifts are larger. Hydrophobic pores lead to larger q_1-values at room temperature while the slopes are more negative.

Fig. 4C shows the slope of the linearly fitted peak shift against the pore diameter. For individual samples, a trend of the slope deviating further from bulk water in smaller pores can be observed. This trend seems to be stronger between the hydrophilic pores than the more hydrophobic ones. BTEVA(4.3) shows a slope closer to bulk water and the hydrophobic samples than to BTEVA(3.8) and BTEVA(3.4). In the hydrophobic samples, no such trend can be observed. In fact, they seem to show a decrease of the slope for smaller pore diameters, notably even between BTEVFB(4.9) and BTEVFB(4.4), which only differ in pore size. However, due to the pore size distributions, fitting errors and the small number of measured samples, one should be careful when interpreting this data.

In bulk water, a lower-q position of S1 is often attributed to a larger amount of tetrahedrally structured water.[50,57] While this may also contribute to this effect, this cannot fully be transferred to confined water, as interface and geometric effects become non-negligible in this case. A particularly interesting quantity that is altered in confinement conditions is the density of water. It has been agreed upon that layers with different densities form in water when confined in hydrophilic nanoporous material.[10–12,14,58,59] More molecules adsorb to the pore wall in this case, leading to a higher number density close to the interface and a lower density in the core of the pore. As discussed above, the average density of water throughout the whole pore cross section under confinement in MCM-41 is also considerably lower than that of bulk water.[14,58]

This effect could explain the material-dependent shift of the S1, as it is most prominent in rather hydrophilic pores, with a strong wall-water interaction. As water confined in hydrophobic pores has a larger contact angle with the pore wall, they do not show this decreased density as strongly in comparison to bulk water and therefore we do not observe the S1 shift as strongly as in hydrophilic pores. Furthermore, due to geometric reasons, the negative pressure could scale with smaller pore diameters. This might lead to the effect being more pronounced in smaller pores than in larger ones, which is also reflected in the S1 shift we observed. The interplay of pore size and hydrophilicity seems to induce a very low density in BTEVP(3.5), which would be even lower than that of LDA. It is surprising, that confinement in BTEVP(3.5) seems to lead to a density in liquid water that is even lower than that of LDA and especially low at room temperature. Note that while the density cannot completely be identified via the structure factor, a smaller density would certainly lead to smaller values of q_1[14] and is therefore in agreement with the data presented here, as well as previous studies.[14,54,55]

Pair Distribution Function For completion, Figure 5A shows the structure factors at the highest and lowest studied temperatures. In Figure 5B the computed pair distribution functions (PDFs) for water in the various PMO materials are plotted once at the highest studied temperature T_{max} and once at the lowest T_{min}. T_{max} and T_{min} for each sample are noted in the individual plots in Figure 5C. For bulk water, $T_{\text{max}} = 295.1\,\text{K}$ and $T_{\text{min}} = 254.1\,\text{K}$.[50]

Figure 5B reveals qualitative differences in the structure of confined water compared to bulk that are present in all PMO materials. The most striking one is the splitting of the broad second neighbour peak of bulk water into several seperate ones. In MCM-41(3.9), BTEVA(3.8), BTEVA(3.4) and BTEVP(3.5), two peaks are present in this region, while the rest of the samples cause three peaks.

The appearance of several peaks emerging in the region from 3.5 to 5 Å can be attributed to a more pronounced, albeit distorted, tetrahedrally bonded network, which has also been observed in previous studies for (hydrophilically) confined water.[14–16,58] While the broad peak in bulk water suggests a broad distribution of second-neighbour distances, the two peaks present in the previously mentioned samples would hint at two more discrete distances. The emergence of a third peak may indicate a more bulk-like behaviour in these materials, such that the number of possible second-neighbour bonding lengths is increased in comparison to the samples giving only two peaks. The results presented in Fig. 5B are consistent with literature,[14–16,58] as two peaks are predominantly present in smaller and more hydrophilic pores and three peaks in larger, as well as more hydrophobic pores.

Running Coordination Number The analysis of the pair distribution functions gave a first hint towards the presence of tetrahedral structuring in the confined water. To gain more insight into this, we take a look into account the interstitial molecules between the first and second neighbour peaks. These can be visualized by integrating the radial distribution

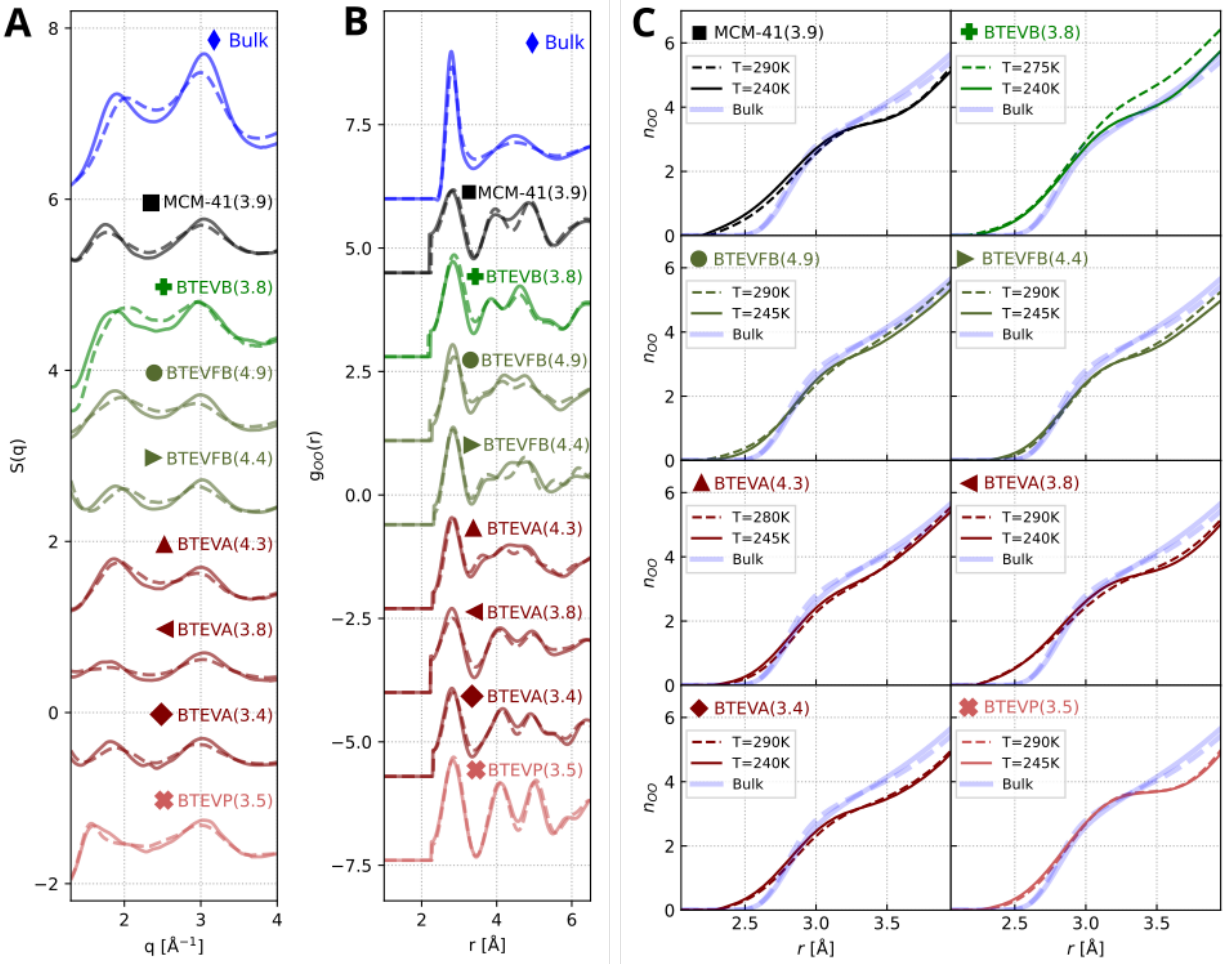

Figure 5: **A** Structure factor of water in the observed samples at the highest as well as the lowest used temperature. The data for bulk water was measured by Pathak *et al.*[53] The curves are set 1 unit apart of each other. **B** The pair distribution functions at the same temperatures. $g_{OO}(r < 2.2\,\text{Å})$ were set to zero, as signal in this range comes from artifacts of the correlation. Bulk data is from Skinner et al.[60] The curves are set 1.7 units apart of each other. **C** The running coordination number of water in the samples.

function. The subsequent quantity is called the running coordination number n_{OO}.[14,52,53] The resulting curves for n_{OO} versus the distance from an initial oxygen atom are shown in Fig. 5C, again at the highest and lowest temperatures for each sample. The curve for bulk water is also shown in blue for comparison. More or less pronounced plateaus are observed around 3.5 Å in all samples, as well as in bulk water. A more strongly pronounced plateau can be attributed to more tetrahedral structuring, as it indicates less or no interstitial oxygen atoms between the first and second neighbour shells.[53] From this we can derive another qualitative statement about the presence of tetrahedrally structured water in the various confining materials. The curves of BTEVA(3.8), BTEVA(3.4) and especially BTEVP(3.5) and MCM-41(3.9) show a strongly pronounced plateau, indicating a larger ratio of tetrahedral water when compared to bulk water. Water confined in the remaining materials shows a more bulk-like plateau, indicating a more disordered water structure in these materials. These results are again in agreement with the previously discussed findings that (hydrophilic) confinement supports the formation of a tetrahedrally structured hydrogen bond network.[14–16,58]

Discussion

We observed that the structural behaviour of water under confinement in PMOs is strongly influenced by the properties of the confining material. In particular, the shift of the first structure factor peak of water during cooling differs more strongly from bulk water in hydrophilic pores than in more hydrophobic pores. This effect can be attributed to a lower density of the confined water compared to bulk. We could also show that by lowering the pore diameter, this effect can be further amplified.

In the PDFs of water in the PMOs, a distinction can be observed between materials which lead to either two and three peaks in the region of 3.5 to 5.5 Å, *i.e.* the region of the second neighbour peak in the PDF of bulk water. While smaller pores give two distinct peaks, confinement in larger pores leads to three peaks or no clear peak structure at all. The presence of two peaks is attributed to the development of a distorted tetrahedral bonding structure,[14,15,58] while the presence of a third peak could hint at the restoration of more bulk-like conditions. Looking at the minimum between the first and second PDF peak, as well as the running coordination number, we could furthermore observe a higher amount of tetrahedral structuring in smaller and more hydrophilic pores. In constrast, larger and more hydrophobic pores show a weaker development of tetrahedral structures. This is in agreement with conclusions from previous studies, which also observe that hydrophilic confinement supports tetrahedral structuring.[14–16]

We can conclude that by confinement in PMOs with varying pore diameters and pore wall chemistry, it is possible to tune fundamental properties of water, such as density and amount of tetrahedral structuring. Further experimental and simulation studies would be beneficial to acquire a more in-depth understanding of these effects.

Acknowledgement

We acknowledge DESY (Hamburg, Germany), a member of the Helmholtz Association HGF, for the provision of experimental facilities. Parts of this research were carried out at PETRA III and we would like to thank Dr. Alexander Schökel and Dr. Martin Etter for assistance in using the P02.1 beamline.[46] Beamtime was allocated for proposals I-20200440 and I-20190201.

This research was carried out in the framework of the city of Hamburg's state funded research project (LFF) "Control of the special properties of water in nanopores". It was furthermore supported by the Centre for Molecular Water Science (CMWS) in an Early Science Project and by the Cluster of Excellence Advanced Imaging of Matter of the Deutsche Forschungsgemeinschaft (DFG) (EXC 2056, Project 390715994).

References

(1) Jähnert, S.; Chávez, F. V.; Schaumann, G.; Schreiber, A.; Schönhoff, M.; Findenegg, G. Melting and freezing of water in cylindrical silica nanopores. *Phys. Chem. Chem. Phys.* **2008**, *10*, 6039–6051.

(2) Deschamps, J.; Audonnet, F.; Brodie-Linder, N.; Schoeffel, M.; Alba-Simionesco, C. A thermodynamic limit of the melting/freezing processes of water under strongly hydrophobic nanoscopic confinement. *Phys. Chem. Chem. Phys.* **2010**, *12*, 1440–1443.

(3) Jelassi, J.; Castricum, H. L.; Bellissent-Funel, M.-C.; Dore, J.; Webber, J. B. W.; Sridi-Dorbez, R. Studies of water and ice in hydrophilic and hydrophobic mesoporous silicas: pore characterisation and phase transformations. *Phys. Chem. Chem. Phys.* **2010**, *12*, 2838–2849.

(4) Moore, E. B.; Allen, J. T.; Molinero, V. Liquid-ice coexistence below the melting temperature for water confined in hydrophilic and hydrophobic nanopores. *J. Phys. Chem. C* **2012**, *116*, 7507–7514.

(5) Thompson, W. H. Solvation dynamics and proton transfer in nanoconfined liquids. *Annu. Rev. Phys. Chem.* **2011**, *62*, 599–619.

(6) Reiter, G.; Deb, A.; Sakurai, Y.; Itou, M.; Krishnan, V.; Paddison, S. Anomalous ground state of the electrons in nanoconfined water. *Phys. Rev. Lett.* **2013**, *111*, 036803.

(7) Kapoor, K.; Patil, S., *et al.* Viscoelasticity and shear thinning of nanoconfined water. *Phys. Rev. E* **2014**, *89*, 013004.

(8) Munoz-Santiburcio, D.; Marx, D. Chemistry in nanoconfined water. *Chem. Sci.* **2017**, *8*, 3444–3452.

(9) Liang, C.; Rayabharam, A.; Aluru, N. Structural and Dynamical Properties of H2O and D2O under Confinement. *J. Phys. Chem. B* **2023**, *127*, 6532–6542.

(10) Gallo, P.; Ricci, M.; Rovere, M. Layer analysis of the structure of water confined in vycor glass. *J. Chem. Phys.* **2002**, *116*, 342–346.

(11) Gallo, P.; Rovere, M.; Chen, S.-H. Dynamic crossover in supercooled confined water: Understanding bulk properties through confinement. *J. Phys. Chem. Lett.* **2010**, *1*, 729–733.

(12) Soper, A. K. Density profile of water confined in cylindrical pores in MCM-41 silica. *J. Phys. Condens. Matter* **2012**, *24*, 064107.

(13) Erko, M.; Wallacher, D.; Hoell, A.; Hauss, T.; Zizak, I.; Paris, O. Density minimum of confined water at low temperatures: a combined study by small-angle scattering of X-rays and neutrons. *Phys. Chem. Chem. Phys.* **2012**, *14*, 3852–3858.

(14) Soper, A. K. Radical re-appraisal of water structure in hydrophilic confinement. *Chem. Phys. Lett.* **2013**, *590*, 1–15.

(15) Smirnov, P.; Yamaguchi, T.; Kittaka, S.; Takahara, S.; Kuroda, Y. X-ray diffraction study of water confined in mesoporous MCM-41 materials over a temperature range of 223- 298 K. *J. Phys. Chem. B* **2000**, *104*, 5498–5504.

(16) Khoder, H.; Schaniel, D.; Pillet, S.; Bendeif, E.-E. X-ray scattering study of water confined in bioactive glasses: experimental and simulated pair distribution function. *Acta Crystallogr. A* **2020**, *76*, 589–599.

(17) Crupi, V.; Interdonato, S.; Longo, F.; Majolino, D.; Migliardo, P.; Venuti, V. A new insight on the hydrogen bonding structures of nanoconfined water: a Raman study. *J. Raman spectrosc.* **2008**, *39*, 244–249.

(18) Malfait, B.; Moréac, A.; Jani, A.; Lefort, R.; Huber, P.; Fröba, M.; Morineau, D. Structure of water at hydrophilic and hydrophobic interfaces: Raman spectroscopy of

water confined in periodic mesoporous (organo) silicas. *J. Phys. Chem. C* **2022**, *126*, 3520–3531.

(19) Inagaki, S.; Guan, S.; Ohsuna, T.; Terasaki, O. An ordered mesoporous organosilica hybrid material with a crystal-like wall structure. *Nature* **2002**, *416*, 304–307.

(20) Sayari, A.; Wang, W. Molecularly ordered nanoporous organosilicates prepared with and without surfactants. *J. Am. Chem. Soc.* **2005**, *127*, 12194–12195.

(21) Cornelius, M.; Hoffmann, F.; Fröba, M. Periodic mesoporous organosilicas with a bifunctional conjugated organic unit and crystal-like pore walls. *Chem. Mater.* **2005**, *17*, 6674–6678.

(22) Beretta, M.; Morell, J.; Sozzani, P.; Fröba, M. Towards peptide formation inside the channels of a new divinylaniline-bridged periodic mesoporous organosilica. *Chem. Commun.* **2010**, *46*, 2495–2497.

(23) Waki, M.; Mizoshita, N.; Ohsuna, T.; Tani, T.; Inagaki, S. Crystal-like periodic mesoporous organosilica bearing pyridine units within the framework. *Chem. Commun.* **2010**, *46*, 8163–8165.

(24) Bracco, S.; Beretta, M.; Cattaneo, A.; Comotti, A.; Falqui, A.; Zhao, K.; Rogers, C.; Sozzani, P. Dipolar rotors orderly aligned in mesoporous fluorinated organosilica architectures. *Angew. Chem., Int. Ed.* **2015**, *54*, 4773–4777.

(25) Martens, S.; Ortmann, R.; Brieler, F. J.; Pasel, C.; Joo Lee, Y.; Bathen, D.; Fröba, M. Periodic mesoporous organosilicas as adsorbents of toxic trace gases out of the ambient air. *Z. anorg. allg. Chem.* **2014**, *640*, 632–640.

(26) Mietner, J. B. Visiting nanopores: The great potential of PMOs for studying the properties of water in nanopores of different polarity. Ph.D. thesis, 2018.

(27) Mietner, B. J.; Fröba, M.; Valiullin, R. Water Transport in Periodic Mesoporous Organosilica Materials. *J. Phys. Chem. C* **2018**, *122*, 12673–12680.

(28) Jani, A.; Busch, M.; Mietner, J. B.; Ollivier, J.; Appel, M.; Frick, B.; Zanotti, J.-M.; Ghoufi, A.; Huber, P.; Fröba, M. *et al.* Dynamics of water confined in mesopores with variable surface interaction. *J. Chem. Phys.* **2021**, *154*, 094505.

(29) Yang, Q.; Liu, J.; Zhang, L.; Li, C. Functionalized periodic mesoporous organosilicas for catalysis. *J. Mater. Chem.* **2009**, *19*, 1945–1955.

(30) Karimi, B.; Mirzaei, H. M.; Mobaraki, A. Periodic mesoporous organosilica functionalized sulfonic acids as highly efficient and recyclable catalysts in biodiesel production. *Catal. Sci. Technol.* **2012**, *2*, 828–834.

(31) Parambadath, S.; Mathew, A.; Barnabas, M. J.; Ha, C.-S. A pH-responsive drug delivery system based on ethylenediamine bridged periodic mesoporous organosilica. *Microporous Mesoporous Mat.* **2015**, *215*, 67–75.

(32) Rao, K. M.; Parambadath, S.; Kumar, A.; Ha, C.-S.; Han, S. S. Tunable intracellular degradable periodic mesoporous organosilica hybrid nanoparticles for doxorubicin drug delivery in cancer cells. *ACS Biomater. Sci. Eng.* **2018**, *4*, 175–183.

(33) Inagaki, S.; Ohtani, O.; Goto, Y.; Okamoto, K.; Ikai, M.; Yamanaka, K.-i.; Tani, T.; Okada, T. Light harvesting by a periodic mesoporous organosilica chromophore. *Angew. Chem.* **2009**, *121*, 4102–4106.

(34) Takeda, H.; Ohashi, M.; Goto, Y.; Ohsuna, T.; Tani, T.; Inagaki, S. Light-Harvesting Photocatalysis for Water Oxidation Using Mesoporous Organosilica. *Chem. Eur. J.* **2014**, *20*, 9130–9136.

(35) Croissant, J. G.; Cattoën, X.; Man, M. W. C.; Durand, J.-O.; Khashab, N. M. Syntheses

and applications of periodic mesoporous organosilica nanoparticles. *Nanoscale* **2015**, *7*, 20318–20334.

(36) Mietner, J. B.; Brieler, F. J.; Lee, Y. J.; Fröba, M. Properties of water confined in periodic mesoporous organosilicas: nanoimprinting the local structure. *Angew. Chem., Int. Ed.* **2017**, *56*, 12348–12351.

(37) Malfait, B.; Jani, A.; Mietner, J. B.; Lefort, R.; Huber, P.; Fröba, M.; Morineau, D. Influence of pore surface chemistry on the rotational dynamics of nanoconfined water. *J. Phys. Chem. C* **2021**, *125*, 16864–16874.

(38) Bilo, M. Controlled pore glasses and alginate hydrogels as form-giving matrices for nanoporous organosilicas. Ph.D. thesis, 2019.

(39) Feng, J.; Zhang, C.; Li, Y.; Yang, M. Hyperbranched polymer based on triphenylamine and pyridine: Fluorescent chemosensors for palladium ions. *J. Appl. Polym. Sci.* **2011**, *121*, 217–225.

(40) Brunauer, S.; Emmett, P. H.; Teller, E. Adsorption of gases in multimolecular layers. *J. Am. Chem. Soc.* **1938**, *60*, 309–319.

(41) Landers, J.; Gor, G. Y.; Neimark, A. V. Density functional theory methods for characterization of porous materials. *Colloids Surf. A* **2013**, *437*, 3–32.

(42) Thommes, M.; Kaneko, K.; Neimark, A. V.; Olivier, J. P.; Rodriguez-Reinoso, F.; Rouquerol, J.; Sing, K. S. Physisorption of gases, with special reference to the evaluation of surface area and pore size distribution (IUPAC Technical Report). *Pure and applied chemistry* **2015**, *87*, 1051–1069.

(43) Fried, D. I.; Bednarski, D.; Dreifke, M.; Brieler, F. J.; Thommes, M.; Fröba, M. Influence of the hydrophilic–hydrophobic contrast of porous surfaces on the enzymatic performance. *J. Mater. Chem. B* **2015**, *3*, 2341–2349.

(44) Thommes, M.; Mitchell, S.; Perez-Ramirez, J. Surface and pore structure assessment of hierarchical MFI zeolites by advanced water and argon sorption studies. *J. Phys. Chem. C* **2012**, *116*, 18816–18823.

(45) Thommes, M.; Morell, J.; Cychosz, K. A.; Fröba, M. Combining nitrogen, argon, and water adsorption for advanced characterization of ordered mesoporous carbons (CMKs) and periodic mesoporous organosilicas (PMOs). *Langmuir* **2013**, *29*, 14893–14902.

(46) Dippel, A.-C.; Liermann, H.-P.; Delitz, J. T.; Walter, P.; Schulte-Schrepping, H.; Seeck, O. H.; Franz, H. Beamline P02. 1 at PETRA III for high-resolution and high-energy powder diffraction. *J. Synchrotron Radiat.* **2015**, *22*, 675–687.

(47) Amann-Winkel, K.; Bellissent-Funel, M.-C.; Bove, L. E.; Loerting, T.; Nilsson, A.; Paciaroni, A.; Schlesinger, D.; Skinner, L. X-ray and neutron scattering of water. *Chem. Rev.* **2016**, *116*, 7570–7589.

(48) Juhás, P.; Davis, T.; Farrow, C. L.; Billinge, S. J. PDFgetX3: a rapid and highly automatable program for processing powder diffraction data into total scattering pair distribution functions. *J. Appl. Crystallogr.* **2013**, *46*, 560–566.

(49) Egami, T.; Billinge, S. J. *Underneath the Bragg peaks: structural analysis of complex materials*; Newnes, 2012; Chapter 5.

(50) Sellberg, J. A.; Huang, C.; McQueen, T. A.; Loh, N.; Laksmono, H.; Schlesinger, D.; Sierra, R.; Nordlund, D.; Hampton, C.; Starodub, D. *et al.* Ultrafast X-ray probing of water structure below the homogeneous ice nucleation temperature. *Nature* **2014**, *510*, 381–384.

(51) Benmore, C.; Gallington, L. C.; Soignard, E. Intermediate range order in supercooled water. *Mol. Phys.* **2019**, *117*, 2470–2476.

(52) Mariedahl, D.; Perakis, F.; Späh, A.; Pathak, H.; Kim, K. H.; Camisasca, G.; Schlesinger, D.; Benmore, C.; Pettersson, L. G. M.; Nilsson, A. *et al.* X-ray scattering and O–O pair-distribution functions of amorphous ices. *J. Phys. Chem. B* **2018**, *122*, 7616–7624.

(53) Pathak, H.; Späh, A.; Kim, K. H.; Tsironi, I.; Mariedahl, D.; Blanco, M.; Huotari, S.; Honkimäki, V.; Nilsson, A. Intermediate range O–O correlations in supercooled water down to 235 K. *J. Chem. Phys.* **2019**, *150*, 224506.

(54) Yoshida, K.; Yamaguchi, T.; Kittaka, S.; Bellissent-Funel, M.-C.; Fouquet, P. Thermodynamic, structural, and dynamic properties of supercooled water confined in mesoporous MCM-41 studied with calorimetric, neutron diffraction, and neutron spin echo measurements. *J. Chem. Phys.* **2008**, *129*, 054702.

(55) Kamitakahara, W. A.; Faraone, A.; Liu, K.-H.; Mou, C.-Y. Temperature dependence of structure and density for D2O confined in MCM-41-S. *J. Phys. Condens. Matter* **2012**, *24*, 064106.

(56) Bowron, D.; Finney, J.; Hallbrucker, A.; Kohl, I.; Loerting, T.; Mayer, E.; Soper, A. The local and intermediate range structures of the five amorphous ices at 80K and ambient pressure: A Faber-Ziman and Bhatia-Thornton analysis. *J. Chem. Phys.* **2006**, *125*, 194502.

(57) Shi, R.; Tanaka, H. Direct evidence in the scattering function for the coexistence of two types of local structures in liquid water. *J. Am. Chem. Soc.* **2020**, *142*, 2868–2875.

(58) Mancinelli, R.; Imberti, S.; Soper, A.; Liu, K.; Mou, C.; Bruni, F.; Ricci, M. A. Multiscale approach to the structural study of water confined in MCM41. *J. Phys. Chem. B* **2009**, *113*, 16169–16177.

(59) Erko, M.; Wallacher, D.; Paris, O. Deformation mechanism of nanoporous materials upon water freezing and melting. *Appl. Phys. Lett.* **2012**, *101*, 181905.

(60) Skinner, L. B.; Benmore, C.; Neuefeind, J. C.; Parise, J. B. The structure of water around the compressibility minimum. *J. Chem. Phys.* **2014**, *141*, 214507.